

Dynamics and resilience of the unconventional charge density wave in ScV₆Sn₆ bilayer kagome metal

Manuel Tuniz^{1,15}, Armando Consiglio^{2,15}, Denny Puntel¹, Chiara Bigi³, Stefan Enzner², Ganesh Pokharel⁴, Pasquale Orgiani⁵, Wibke Bronsch⁶, Fulvio Parmigiani^{1,6}, Vincent Polewczyk⁵, Phil D. C. King³, Justin W. Wells⁷, Ilija Zeljkovic⁸, Pietro Carrara^{5,9}, Giorgio Rossi^{5,9}, Jun Fujii⁵, Ivana Vobornik⁵, Stephen D. Wilson⁴, Ronny Thomale², Tim Wehling^{10,11}, Giorgio Sangiovanni², Giancarlo Panaccione⁵, Federico Cilento⁶✉, Domenico Di Sante^{12,13}✉ & Federico Mazzola^{5,14}✉

Long-range electronic ordering descending from a metallic parent state constitutes a rich playground to study the interplay of structural and electronic degrees of freedom. In this framework, kagome metals are in the most interesting regime where both phonon and electronically mediated couplings are significant. Several of these systems undergo a charge density wave transition. However, to date, the origin and the main driving force behind this charge order is elusive. Here, we use the kagome metal ScV₆Sn₆ as a platform to investigate this problem, since it features both a kagome-derived nested Fermi surface and van-Hove singularities near the Fermi level, and a charge-ordered phase that strongly affects its physical properties. By combining time-resolved reflectivity, first principles calculations and photo-emission experiments, we identify the structural degrees of freedom to play a fundamental role in the stabilization of charge order, indicating that ScV₆Sn₆ features an instance of charge order predominantly originating from phonons.

¹Dipartimento di Fisica, Università degli studi di Trieste, Trieste 34127, Italy. ²Institut für Theoretische Physik und Astrophysik and Würzburg-Dresden Cluster of Excellence ct.qmat, Universität Würzburg, Würzburg 97074, Germany. ³School of Physics and Astronomy, University of St Andrews, St Andrews KY16 9SS, UK. ⁴Materials Department, University of California Santa Barbara, Santa Barbara 93106 CA, USA. ⁵Istituto Officina dei Materiali, Consiglio Nazionale delle Ricerche, Trieste I-34149, Italy. ⁶Elettra - Sincrotrone Trieste S.C.p.A., Trieste Strada Statale 14, km 163.5 Italy. ⁷Centre for Materials Science and Nanotechnology, University of Oslo (UiO), Oslo 0318, Norway. ⁸Department of Physics, Boston College, Chestnut Hill 02467 MA, USA. ⁹Dipartimento di Fisica, Università degli Studi di Milano, Milano via Celoria 16, 20133, Italy. ¹⁰Institute of Theoretical Physics, University of Hamburg, Hamburg Notkestrasse 9, 22607, Germany. ¹¹The Hamburg Centre for Ultrafast Imaging, Hamburg Luruper Chaussee 149, 22761, Germany. ¹²Department of Physics and Astronomy, University of Bologna, Bologna 40127, Italy. ¹³Center for Computational Quantum Physics, Flatiron Institute, Bologna, 162 5th Avenue, New York 10010 NY, USA. ¹⁴Department of Molecular Sciences and Nanosystems, Ca' Foscari University of Venice, Venice 30172, Italy. ¹⁵These authors contributed equally: Manuel Tuniz and Armando Consiglio. ✉email: federico.cilento@elettra.eu; domenico.disante@unibo.it; federico.mazzola@unive.it

Bilayer kagome metals are an emerging class of correlated topological compounds with chemical formula RV_6Sn_6 (R : rare earth - hereafter also dubbed as the 166 family), featuring unconventional topological phases and collective magnetic excitations at low temperature^{1–11}. Similarly to the sister compounds AV_3Sb_5 ^{4,5,12–15} (A : alkali atoms - hereafter also nicknamed as the 135 family), the electronic structure of RV_6Sn_6 is a rich platform for the emergence of unconventional phase diagrams, boasting the simultaneous presence of itinerant Dirac electrons, non-trivial flat bands, and van-Hove singularities at the Fermi energy (E_F)^{12–20}. Among the 166 family, ScV_6Sn_6 exhibits a unique and unconventional charge density wave (CDW) transition^{21–24}, characterized by the softening of an extremely flat phonon mode²¹, the competition between two order parameters²² and a motif dissimilar to those observed in other kagome compounds^{6,25}. On the kagome lattice in general, the CDW phase provokes an atomic displacement which might generate unconventional phenomena, such as metal-insulator transitions of fermions, vortices at the surface, chiral currents, and bond orders^{6,18,26–32}. One of the major goals of contemporary research about kagome metals is thus to reveal the underlying mechanism of the charge order in ScV_6Sn_6 and the specific role of structural and electronic degrees of freedom, the interdependence of whom has so far remained uncharted territory.

Previous works have highlighted differences and similarities between ScV_6Sn_6 , AV_3Sb_5 , and $FeGe$ ³³. In particular, in AV_3Sb_5 , the charge order has been thought to be connected to the nesting of the Fermi surface, exemplified by the van-Hove singularity electron filling^{25,34–36}. Such a nesting is a hallmark of the vast majority of kagome metals, including ScV_6Sn_6 . However, in AV_3Sb_5 , the charge order has been conjectured to be linked to the emergence of superconductivity and stripe orders^{32,37–42}, while ScV_6Sn_6 does not undergo any superconducting transition at low temperature. In addition, for the latter, the CDW, generated by the ordering vector $\mathbf{Q} = (1/3, 1/3, 1/3)$, does not give rise to either the Star of David or trihexagonal arrangement, as for the AV_3Sb_5 compounds, for which the ordering vectors are $\mathbf{Q} = (1/2, 1/2, 1/4)$ and $\mathbf{Q} = (1/2, 1/2, 1/2)$ ^{36,43,44}. Other differences between these two systems, are also reflected in a much more rapid CDW suppression for ScV_6Sn_6 under the application of pressures⁴⁵, offering an increased ease of tuneability compared to AV_3Sb_5 . However, despite the differences, there are important similarities between all kagome metals. These similarities have been conjectured as possible cause of the CDW transition, and are, namely, the van-Hove singularities in proximity of the Fermi level and also a nested Fermi surface. Understanding the origin of the CDW in a simpler system without superconducting transition could be therefore of great help in elucidating the role of such kagome-derived features in driving the CDW phase.

In CDW materials, the simultaneous occurrence of a lattice displacement and a change in the electronic structure, often associated with the opening of gaps in the electronic spectrum challenges the understanding of the main driving force behind the charge order and limits the access to possible consequent or concomitant cascade of collective phases and their control. While there is compelling evidence of CDW in kagome systems, its microscopic origin and dynamics are still debated. We stress that the understanding of such origin and dynamics is a task of central importance given the peculiar electronic structure of kagome with van-Hove singularities at the Fermi level and the presence of a nested Fermi surface, which hints at an energy gain upon a gap opening as an underlying driver. For the 166, which has also a topological nature, it becomes crucial to understand the dynamics of the CDW, to uncover not only the relationship between subsequent ordered phases, but also to elucidate the interplay between the phase transition and the topological aspects^{5,36,46–49}.

In the present study, we use time-resolved optical spectroscopy (TR-OS), angle-resolved photoemission spectroscopy (ARPES) and density functional theory (DFT) calculations, to unveil the dynamics of the CDW in the 166 bilayer kagome ScV_6Sn_6 . Specifically, we disclose the energy scales involved in the charge order, which points towards a major robustness of the lattice degree of freedom for the observed transition.

Results and discussion

Electronic structure of ScV_6Sn_6 . Firstly, we describe the electronic properties of ScV_6Sn_6 , then we will show by using ARPES, first-principles calculations, and TR-OS how the electronic and structural degrees of freedom are affected by the CDW order. Along with the crystal structure (both with and without CDW) and the Brillouin zone (Fig. 1a in the absence of CDW; Fig. 1c in the presence of CDW; Fig. 1b is the system's Brillouin zone), we show the expected electronic structure from DFT, above and below the transition temperature, in Fig. 1d (red color without CDW, green shades with CDW). In both the ordered and pristine cases, the Dirac-like states and the van-Hove singularities are similar and identifiable, with negligible variation in their electronic dispersion along the Γ - K - M - Γ path. Such a negligible change is fully consistent with our ARPES spectra collected along the same direction and shown in Supplementary Fig. 1c, d (above T_{CDW}) and g–h (below T_{CDW}). Also the corresponding Fermi surfaces (see Supplementary Note 1, in particular Supplementary Fig. 1a, b for above T_{CDW} and e–f for below T_{CDW}) displays negligible changes. According to our DFT calculations (Fig. 1d), one can expect the largest effects of the CDW to occur along the bulk A–L direction (where in our experimental geometry ARPES matrix elements are rather unfavorable - see also Supplementary Figs 1–6), that projects onto the surface $\bar{\Gamma}$ - \bar{M} direction. Our ARPES data appear consistent with ref. ²⁴: The spectra collected along $\bar{\Gamma}$ - \bar{M} for both above (Fig. 2a) and below T_{CDW} (Fig. 2b) reveal the opening of a clear energy gap, the hallmark of the CDW transition of this system. Such a gap, that mostly affects a single band, can be appreciated also by looking at the energy-distribution curves (EDCs) extracted around $k_y = 0.5\text{\AA}^{-1}$ and shown in Fig. 2e: the red curve, referring to the EDC extracted for the data at temperatures below the CDW transition, presents an evident peak centered around 200 meV below the Fermi level. On the contrary, this does not occur for the data above T_{CDW} . Evidence of the gap opening can be additionally seen in the curvature of the ARPES spectra, shown in Fig. 2c, d. Despite the direct observation of the gap in ARPES, the origin of the CDW is yet unknown.

For completeness, it is worth mentioning that ScV_6Sn_6 , similarly to other kagome metals, is characterized by the presence of surface states, after the ultrahigh vacuum (UHV) cleave (see Methods for details about the samples' preparation). These surface states have been extensively discussed for other kagome systems^{12,13,35}, other members of the 166 family^{4,5,7–9,50}, and also recently reported for ScV_6Sn_6 ²⁴. By comparing our results with those of ref. ²⁴, we found a surface termination consistent with the spectral weight of a V_3Sn area: the surface states at the K -points (not observed for the $ScSn_2$ termination), the vanishing intensity of the parabolic states close to the quadratic minimum (see 'qm' in Supplementary Fig. 1c and g), and the absence of the small pocket at $\bar{\Gamma}$ and at the Fermi level observed for the Sn_2 termination, are all good evidence of this attribution²⁴. In order to better distinguish between surface and bulk electronic structure, for completeness, we also measured the sample after having suppressed such surface states (see Supplementary Figs. 2–7 and Supplementary Notes 2, 3). It is crucial to point out that the type of surface termination obtained after the cleave is irrelevant to our study, having the CDW a marked bulk character.

ScV₆Sn₆ shows a very peculiar ordered phase, with a marked peak in the specific heat and an increased metallic character below the transition⁶. However, the origin of the charge order is still an open question. It is then crucial to separate the time- and energy-scales of the electronic and lattice degrees of freedom and to determine their robustness and involvement in the CDW order.

Influence of CDW order on the electronic and structural degrees of freedom. Aiming to answer to the conclusive point raised in the last subsection, we use TR-OS and we measure the

time-resolved reflectivity dynamics of ScV₆Sn₆. Fig. 3a presents the temperature (T) dependence of the photoinduced reflectivity transients, $\Delta R/R$, recorded upon increasing the temperature (T from approximately 18 K; the fluence was $F \approx 0.2 \text{ mJ cm}^{-2}$). The $\Delta R/R$ can be described by two features: an incoherent (non-oscillating) response and a coherent oscillatory behavior. In our data, clear oscillations in the $\Delta R/R$, showing a strong T-dependence, are detected up to the transition temperature T_{CDW} (Fig. 3a, b). The incoherent (non-oscillating) response consists of two decays, a fast and a slow

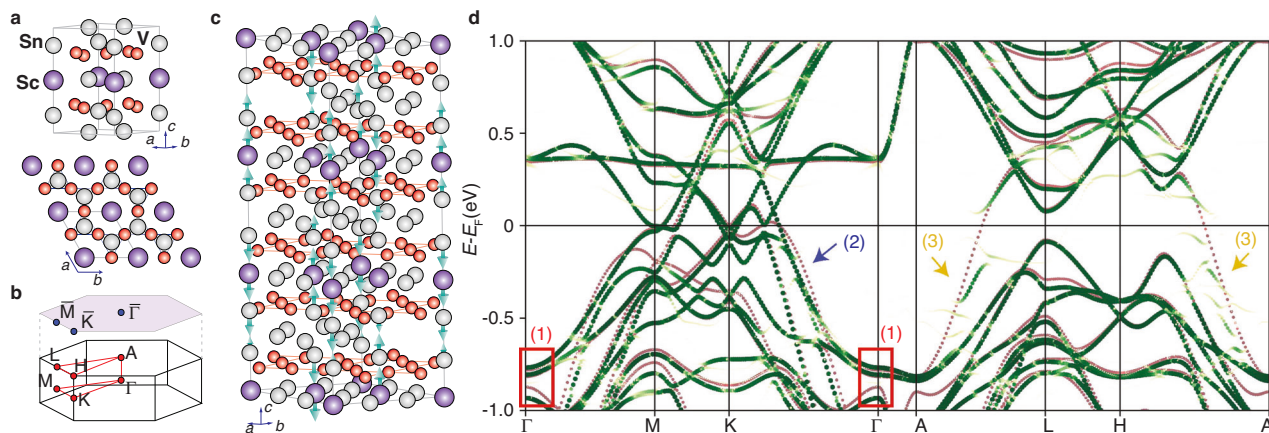


Fig. 1 Crystal and calculated electronic structure of ScV₆Sn₆. **a** Crystal structure without CDW. The top-view corresponds to a 2×2 cell. **b** Brillouin Zone with high-symmetry points and directions. **c** Crystal structure in the CDW phase with the out-of-plane distortions indicated by the arrows. The length of the arrow is proportional to the displacement. **d** Electronic structure of ScV₆Sn₆ without (red lines) and with CDW (green color) along the high symmetry directions. For visual clarity, the pristine bands have been translated in energy by $+0.029 \text{ eV}$. In this way the van-Hove singularities and the d_{z^2} flat band of the CDW and pristine systems are aligned. It is indeed expected that a structural distortion leads to a tuning in the electronic band structure, especially around E_F ⁷⁶. A similar but disentangled figure can be found in Supplementary Fig. 9. The main changes are here indicated: at $\bar{\Gamma}$ (red box, label '1') the CDW induces an increment in the bands separation. Along both $\bar{\Gamma}-\bar{K}$ and $\bar{\Gamma}-\bar{M}$ the bands appear to have slightly different k -loci (blue arrow and label '2'). The main changes are observed along the A-H and A-L directions (yellow arrows and label '3') and are characterized by a marked Sn p_z -states.

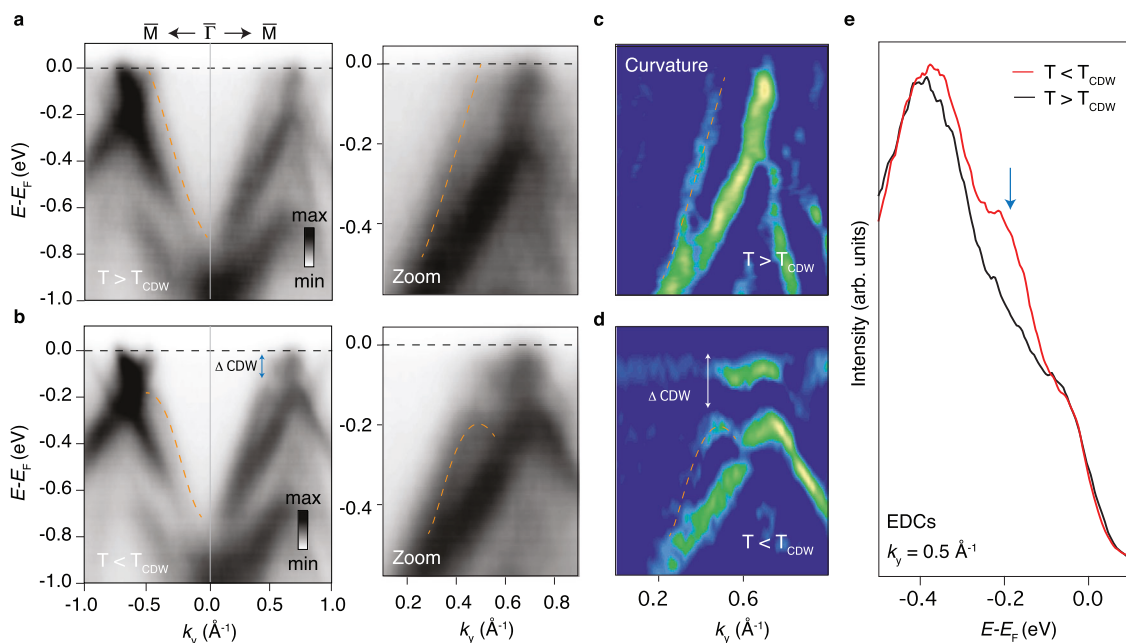


Fig. 2 Measure of the CDW gap across the CDW critical temperature. **a** ARPES measured along the $\bar{M}-\bar{\Gamma}-\bar{M}$ direction above T_{CDW} (and zoomed-in inset). **b** ARPES measured along the $\bar{\Gamma}-\bar{M}$ direction below T_{CDW} (and zoomed-in inset) showing the appearance of an energy gap (see blue arrow). The dashed orange curves are guides for the eye. **c, d** Curvature plots for the ARPES spectra in **(a, b)**, respectively. The difference between **(c, d)** demonstrates the opening of a CDW gap across the transition temperature for the single band highlighted by the orange dashed line. **e** EDCs collected for the ARPES in **(a, b)** taken at approximately 0.5 \AA^{-1} . The red EDC, collected below T_{CDW} , shows a peak around 0.2 eV of binding energy, absent in the case of the black curve collected at a temperature above T_{CDW} .

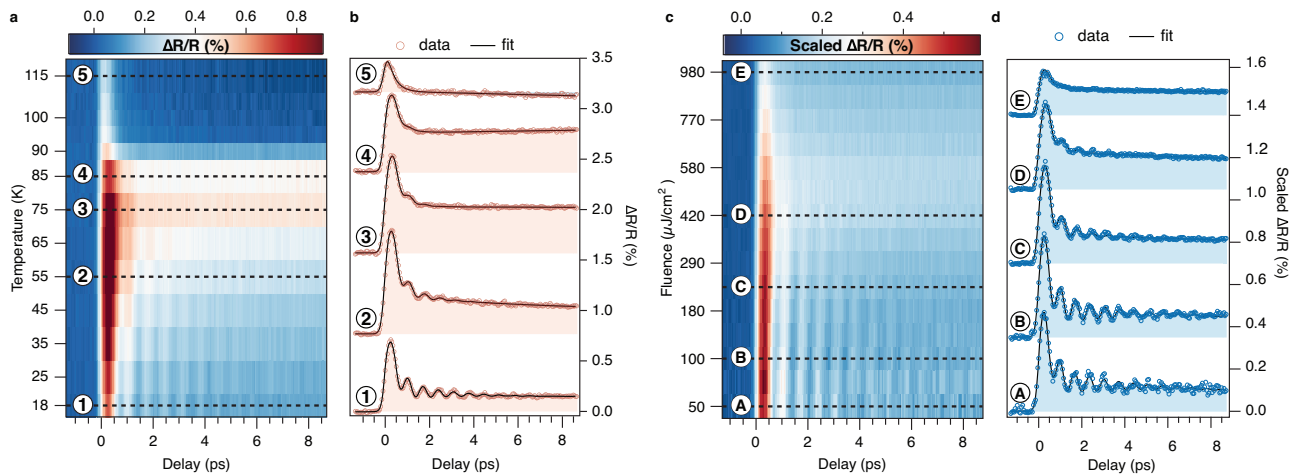


Fig. 3 Temperature and fluence dependent-dynamics of ScV_6Sn_6 . **a** Evolution of $\Delta R/R$ as a function of the temperature in the temperature range across T_{CDW} , showing the signatures of the phase transition around 90 K. In the low temperature CDW phase a clear oscillatory response is observed. **b** $\Delta R/R$ profiles extracted from (a) at selected temperatures, showing the evolution of the dynamics across the phase transition. **c** Evolution of the scaled $\Delta R/R$ as a function of the fluence across T_{CDW} . The traces are scaled to the fluence to ease the visualization upon approaching the photoinduced phase transition. **d** Scaled $\Delta R/R$ profiles extracted from (c) at selected fluences.

one, with characteristic times τ_1 and τ_2 , respectively (see Supplementary Note 4 for details about the data analysis and their extraction) that appear in the data as a fast peak and a slowly-decaying component. Similarly to the coherent response, the incoherent one is also strongly T-dependent and it shows the indication of a phase transition around $T \approx 90$ K (see Fig. 4a), which matches well with the nominal T_{CDW} ⁶. Above T_{CDW} , the $\Delta R/R$ becomes smaller and, after the fast exponential decay, it changes sign becoming negative (see trace '5' of Fig. 3b).

In general, below the CDW critical temperature, the pump pulse induces an abrupt change in the reflectivity, followed by a fast decay within a picosecond and a slower recovery on a timescale of the order ≈ 10 ps^{51–55}. The first, which slows down critically upon approaching the transition temperature, is attributed to the re-opening of the CDW gap, while the second one, as confirmed by detailed studies of the dynamics as a function of the excitation fluence and applied external electric field, is attributed to a second stage of the CDW recovery^{56–59}. In ScV_6Sn_6 , the T-evolution of the incoherent part of the $\Delta R/R$ shows a rather peculiar behavior: in contrast to the well-studied one dimensional CDW systems, the lifetime of the first fast decay τ_1 increases linearly with the temperature and shows a rapid drop at T_{CDW} (Fig. 4a). No divergence of the lifetime τ_1 is observed during the phase transition. This is different from what has been reported for the kagome metal CsV_3Sb_5 , where TR-OS measurements have highlighted the divergence of the lifetime of the fast decay process during the onset of the charge order⁴¹. This peculiar behavior could suggest an unusual origin for the CDW phase in this material.

Interestingly, from the fits to the data (see Supplementary Note 4 and Supplementary Fig. 11 for more details), the frequency of the oscillatory mode and the damping show a pronounced temperature dependence, as we show in Fig. 4b. In particular, at low temperature the mode has a frequency of ~ 1.45 THz, in excellent agreement with our ab-initio estimate of 1.42 THz. The latter is obtained from the quadratic fit of the DFT total energy around the minimum of CDW ordered structure (see Fig. 4c and Methods for more details), and we observe a $\approx 6\%$ softening of the mode frequency and an exponential increase of the damping constant, when the temperature of the system approaches the critical temperature of the CDW transition.

Such a temperature dependence has been observed in many CDW systems and it constitutes the fingerprint of an amplitude mode (AM) of the CDW phase^{54,55,60–63}. This observation confirms that the coherent response is not due to a trivial phonon, but rather to the excitation of the AM of the CDW phase, confirming the onset of CDW physics in ScV_6Sn_6 . We also note that no fingerprints of an AM have been hitherto detected in CsV_3Sb_5 by previous reflectivity studies⁴¹.

By varying the excitation density (fluence), additional information about the nature of the phase transition can be obtained. The melting of the electronic modulation is generally achieved on a timescale much faster than the characteristic timescale related to the relaxation of the periodic lattice modulation, which is given by the period of the characteristic amplitude modes of the system. This results in the disentanglement of electronic and lattice degrees of freedom on the sub-picosecond time scale, with a subsequent rapid recovery of the electronic degrees of freedom^{54,62,64,65}. Additionally, the characteristic energy required to fully drive the phase transition, i.e., quenching the periodic lattice distortion and the electronic degrees of freedom, is that one which leads to the disappearance of the (oscillatory) amplitude mode^{53,64}. This provides a means to quantify the strength of the lattice degree of freedom compared to the electronic one. We report this in Fig. 3c, where the evolution of the scaled $\Delta R/R$ signal as a function of the fluence is shown, in a range from ~ 50 to ~ 1000 $\mu\text{J cm}^{-2}$. The traces are scaled to the fluence to better visualize the qualitative behavior of the response upon approaching the photoinduced phase transition. Note that the sample is kept at a temperature well-below T_{CDW} . In the low perturbation regime, the signal scales linearly with fluence (traces A, B, C in Fig. 3d), while upon approaching the photoinduced phase transition the $\Delta R/R$ signal related to the CDW order shows saturation^{53,64}. The maximum change that can be induced in the signal is generally achieved when the electronic degree of freedom associated to the CDW order is collapsed. We find that the fast electronic component with relaxation time τ_1 saturates at a fluence where the oscillations linked to AM involving the lattice degrees of freedom still persist^{51,64,66}. By progressively increasing the excitation fluence, the oscillations in the $\Delta R/R$ due to the AM get also suppressed, with an exponential increase of the damping constant and a softening of the frequency of the

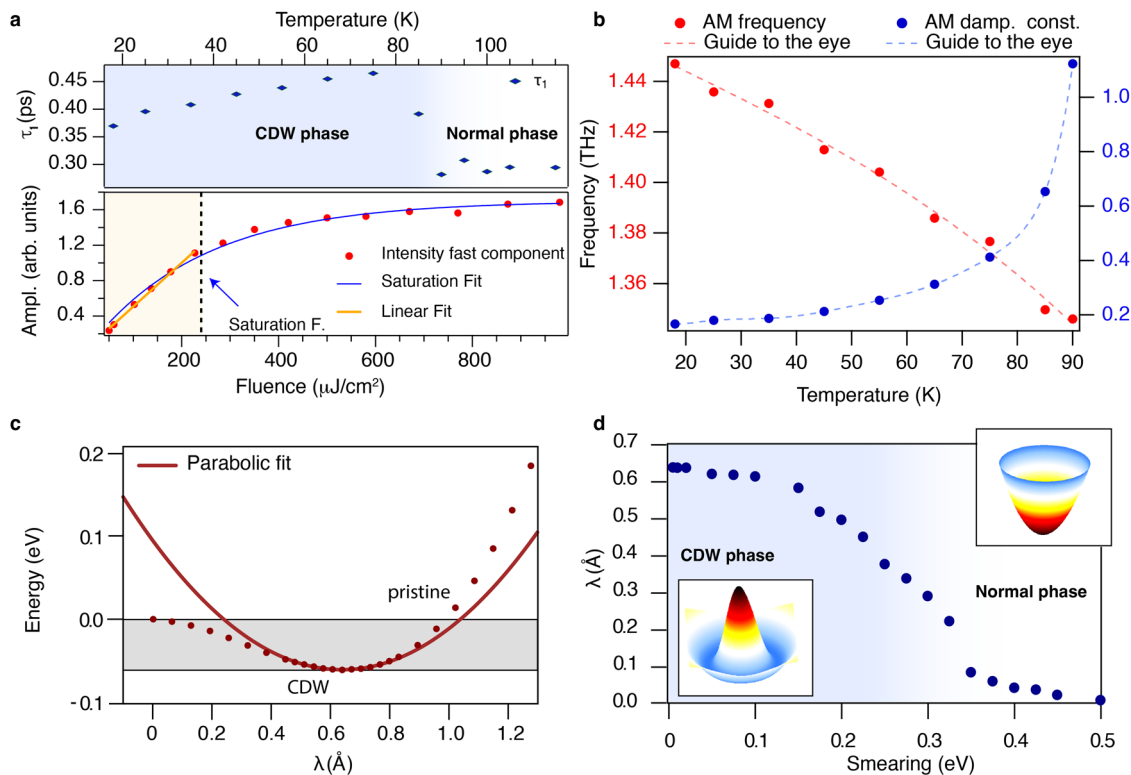


Fig. 4 Evolution of significant fit parameters. **a** Evolution of the lifetime of the first fast decay (τ_1) as a function of the temperature (top panel) and evolution of the amplitude of the fast peak as function of fluence (bottom panel). **b** Evolution of the frequency and the damping constant of the amplitude mode as a function of the temperature. **c** Total energy of the ScV_6Sn_6 constant-volume superlattice while interpolating between the pristine, the CDW and the exaggerated CDW phases. $\lambda = 0.00 \text{ \AA}$ means that the displacement vector has a vanishing norm, i.e., we are in the reference starting point (the pristine phase). When $\lambda = 0.64 \text{ \AA}$, the norm of the displacement vector is $\|\mathbf{e}\| = \lambda$, hence we are in the CDW phase. When further increasing the norm of the displacement vector, we are describing an exaggerated CDW phase. The parabola represented by a continuous line is the quadratic fit of the energy profile, around the minimum. The quadratic coefficient is related to the spring constant k and frequency ω of the CDW amplitude mode (more details in the Methods section). **d** Norm of the 351-dimensional displacement vector $\|\mathbf{e}\|$ among the CDW and pristine structures, as a function of the electronic (gaussian) smearing σ used during the constant-volume ionic relaxation.

mode. Remarkably, our measurements highlight the robustness upon photoexcitation of the lattice reconstruction of the CDW in this material. Indeed, even at high excitation fluences ($\sim 700 \mu\text{J cm}^{-2}$), the oscillations due to the AM are still detected. This behavior is again markedly different from what has been observed in the sister compound CsV_3Sb_5 where, despite the similar CDW critical temperature, already at a pump fluence as small as $\sim 55 \mu\text{J cm}^{-2}$ the CDW order is melted¹. In our study, we show that the oscillation disappears completely only at a fluence of $\sim 1000 \mu\text{J cm}^{-2}$, meaning that the lattice order can be melted, although at a fluence larger than the one required to saturate the purely electronic response at around $\approx 240 \mu\text{J cm}^{-2}$. The electronic states that maximally couple to this CDW span an energy window around the Fermi level of about 0.25 eV, because smearing over that window greatly affects the AM, as we show in Fig. 4d. Indeed, taking into account the electronic specific heat of ScV_6Sn_6 , an absorbed fluence of $\approx 240 \mu\text{J cm}^{-2}$ leads to an increase of the electronic temperature of $\approx 2100 \text{ K}$, which is in reasonable agreement with the smearing obtained by DFT calculations (See Fig. 4 d). Finally, it is only when the average lattice temperature exceeds the CDW critical temperature because of the average power deposited by the pump pulse, that one might expect to detect the transient signal of the high-temperature phase. We estimate the pump-induced average heating to be $\Delta T \approx 20 \text{ K}$ at a fluence of $\approx 1 \text{ mJ cm}^{-2}$. Hence, in order to reach T_{CDW} , very large fluences are required, which are not attainable because sample damage would occur.

Conclusion

In conclusion, by using a combination of experimental techniques, i.e., ARPES and TR-OS, as well as theoretical calculations, we disclose the dynamics of the CDW transition in ScV_6Sn_6 . In particular, temperature dependent TR-OS reveals the hallmarks of the CDW. In addition, our fluence dependent study disentangles the electronic and structural degrees of freedom, showing persisting AM oscillations up to unusually high values of fluence, corroborating the robustness of the lattice distortions compared to the preceding disruption of the purely electronic component. Such behavior is in favor of a CDW with the lattice degrees of freedom and electron-phonon interaction playing the dominant role, in line with recent Raman experiments⁶⁷. This outcome aligns with the likewise recent prediction of the highly unconventional nature of the CDW in ScV_6Sn_6 . The CDW originates in fact from the cooperation of electron-phonon coupling and electron susceptibility, which together contribute to forming the 1-loop electron self-energy correction to the bare phonon propagator that determines the softening of a particularly flat phonon mode^{21,22}. In this respect, predicting the dominant role played by the lattice degrees of freedom, our comprehensive study sheds light onto the collective modes emerging in the low-temperature phase of ScV_6Sn_6 bilayer kagome metal.

Methods

Experimental details. Single crystals of ScV_6Sn_6 were grown using a flux-based growth technique as reported in the ref. ⁶⁸.

Sc (chunk, 99.9%), V (pieces, 99.7%), and Sn (shot, 99.99%) were loaded inside an alumina crucible with the molar ratio of 1:6:20 and then heated at 1125 °C for 12 h. Then, the mixture was slowly cooled to 780 °C at a rate of 2 °C/h. Thin plate-like single crystals were separated from the excess Sn-flux via centrifuging at 780 °C. The samples were cleaved in UHV at the pressure of 1×10^{-10} mbar. The ARPES data were acquired at the APE-LE end station (Trieste) using a VLEED-DA30 hemispherical analyzer. The energy and momentum resolutions were better than 12 meV and 0.02 \AA^{-1} , respectively. The temperature of the measurements was kept constant throughout the data acquisitions (16 K and 120 K, below and above T_{CDW} respectively). Both linear polarizations were used to collect the data from the APE undulator of the synchrotron radiation source ELETTRA (Trieste). The photon energy used for the ARPES data was 75 eV. This choice was such that the spectra intensity was the most prominent, especially near the region of the quadratic minimum of the electronic structure, where the major changes with the CDW are expected.

Time-resolved reflectivity experiments were performed at the T-ReX laboratory (FERMI, in Trieste) with a probe photon energy of $\approx 0.95 \text{ eV}$ (1300 nm). The measurements were performed using a Ti:sapphire femtosecond (fs) laser system, delivering, at a repetition rate of 250 kHz, $\approx 50 \text{ fs}$ light pulses at a wavelength of 800 nm (1.55 eV). The single color probe measurements were performed at a probe wavelength of 1300 nm, obtained by filtering a broadband (0.8–2.3 eV) super-continuum probe beam, generated using a sapphire window.

Theoretical details. DFT calculations have been performed using both Quantum Espresso and VASP packages. Phonon calculations are based on density functional perturbation theory, as implemented in Quantum Espresso^{69–71}. Exchange and correlation effects were included with the generalized gradient approximation using the Perdew-Burke-Ernzerhof functional⁷²; the pseudopotentials are norm-conserving and scalar relativistic, containing core corrections⁷³. Self-consistent calculations and ionic relaxation of the unit cell have been performed with a $9 \times 9 \times 6$ k -grid; convergence threshold for both ionic minimization and electronic self-consistency are set to be 10^{-15} Ry. The kinetic energy cutoff for the wavefunctions is equal to 90 Ry. A ordinary Gaussian spreading of 0.006 Ry has been used. Once the structure was properly at equilibrium, with vanishing forces acting on each atom, we proceeded with the actual phonon calculations. The dynamical matrices have been obtained and computed for a q -grid of $3 \times 3 \times 6$, with a self-consistency threshold of 10^{-15} Ry. These dynamical matrices are consequently Fourier-transformed to obtain the inter-atomic force constants (IFC) in real space; three translational acoustic sum rules have been imposed, via correction of the IFC. Finally, both phonon dispersion and phonon density of states are obtained. In particular, for the density of states calculations (see results in the Supplementary Note 5.) we used $30 \times 30 \times 30$ q -points. The presence of imaginary phonon modes has been verified also for a $6 \times 6 \times 9$ and a $9 \times 9 \times 12$ q -grid, during the dynamical matrices' calculation.

The remaining DFT calculations have been performed with VASP. To study the dependence of the CDW phase with respect to the smearing we used a plane-wave cutoff of 500 eV and a $9 \times 9 \times 9$ Γ -centered k -mesh. Ionic relaxations have been performed with a constant volume. The relaxations of the ionic and electronic degrees of freedom were considered converged respectively below a threshold of 10^{-5} eV and 10^{-10} eV. Subsequently, for each smearing value, we computed the norm of the 351-dimensional ($117 \text{ atoms} \times 3$) displacement vector among the CDW and the pristine phases. Spin-orbit coupling has not been included for this set of calculations.

To study the structural interpolation among the CDW and pristine systems, leading to the double-well potential profile, we computed the 351-dimensional displacement vector \mathbf{e} between the two configurations. This has a norm of $\sim 0.64 \text{ \AA}$. The two structures hence are gradually interpolated, moving the atoms along the direction defined by \mathbf{e} . For each step, a self-consistent calculation with 500 eV for the kinetic energy cutoff and a Γ -centered $12 \times 12 \times 12$ k -grid has been performed. The smearing here is constant and equal to 0.005 eV. The electronic calculations are considered converged below a threshold of 10^{-8} eV. This process has been studied while keeping the volume constant. Also here the spin-orbit coupling has not been included. To compute the frequency of the phonon mode we started from a quadratic fit around the minimum of the Born-Oppenheimer potential, corresponding to the CDW phase; the resulting fit has equation $y = 0.379 \cdot x^2$. From here it is possible to obtain the "spring" constant k , as $k = 2 \times 0.379202 \text{ eV/\AA}^2$. The effective mass m^* is computed using the normalized displacement vector $\mathbf{n} = \mathbf{e} / \|\mathbf{e}\|$ and the mass tensor $\mathbf{M} = \text{diag}(m_1, m_1, m_1, \dots, m_{117}, m_{117}, m_{117})$ via $m^* = \mathbf{e} \cdot (\mathbf{M} \cdot \mathbf{e})$; we obtain $m^* = 91.02 \text{ u}$. Note that this mass value is intermediate among the Sn and Sc ones, i.e., the atoms which mostly participate to the CDW transition. Finally the frequency ν can be computed as $\nu = \omega / (2\pi)$, with $\omega = \sqrt{k/m^*}$, giving us $\nu = 1.42 \text{ THz}$.

When considering the unfolding of the CDW supercell, the Kohn-Sham wave functions are expanded in plane waves up to a 400 eV energy cutoff, with a k -mesh resolution for the self-consistent electronic structure calculations of 0.02 reciprocal Angstroms. For the non-self-consistent calculations, the k -mesh resolution corresponds to 0.01 reciprocal Angstroms. In this case, the spin-orbit coupling has been considered and included self-consistently. The initial CDW supercell corresponds in every case to the experimental one⁶. Band structures have been visualized using the VASPKIT postprocessing tool⁷⁴. VESTA⁷⁵ has been used to visualize the crystal structures.

Data availability

The data that support the findings of this study are available from the corresponding authors upon reasonable request.

Received: 10 October 2023; Accepted: 16 November 2023;

Published online: 04 December 2023

References

1. Wang, Z. X. et al. Unconventional charge density wave and photoinduced lattice symmetry change in the kagome metal CsV_3Sb_5 probed by time-resolved spectroscopy. *Phys. Rev. B* **104**, 165110 (2021).
2. van Heumen, E. Kagome lattices with chiral charge density. *Nat. Mater.* **20**, 1308–1309 (2021).
3. Luo, H. et al. Electronic nature of charge density wave and electron-phonon coupling in kagome superconductor KV_3Sb_5 . *Nat. Commun.* **13**, 273 (2022).
4. Pokharel, G. et al. Electronic properties of the topological kagome metals YV_6Sn_6 and GdV_6Sn_6 . *Phys. Rev. B* **104**, 235139 (2021).
5. Hu, Y. et al. Tunable topological Dirac surface states and van Hove singularities in kagome metal GdV_6Sn_6 . *Sci. Adv.* **8**, eadd2024 (2022).
6. Arachchige, H. W. S. et al. Charge density wave in kagome lattice intermetallic ScV_6Sn_6 . *Phys. Rev. Lett.* **129**, 216402 (2022).
7. Peng, S. et al. Realizing kagome band structure in two-dimensional kagome surface states of RV_6Sn_6 ($R = \text{Gd, Ho}$). *Phys. Rev. Lett.* **127**, 266401 (2021).
8. Ishikawa, H., Yajima, T., Kawamura, M., Mitamura, H. & Kindo, K. GdV_6Sn_6 : a multi-carrier metal with non-magnetic $3d$ -electron Kagome bands and $4f$ -electron magnetism. *J. Phys. Soc. Jpn.* **90**, 124704 (2021).
9. Rosenberg, E. et al. Uniaxial ferromagnetism in the kagome metal TbV_6Sn_6 . *Phys. Rev. B* **106**, 115139 (2022).
10. Lee, J. & Mun, E. Anisotropic magnetic property of single crystals RV_6Sn_6 ($R = \text{Y, Gd - Tm, Lu}$). *Phys. Rev. Mater.* **6**, 083401 (2022).
11. Chen, D. et al. Large anomalous hall effect in the kagome ferromagnet LiMn_6Sn_6 . *Phys. Rev. B* **103**, 144410 (2021).

12. Kang, M. et al. Topological flat bands in frustrated kagome lattice CoSn. *Nat. Commun.* **11**, 4004 (2020).
13. Kang, M. et al. Dirac fermions and flat bands in the ideal kagome metal FeSn. *Nat. Mater.* **19**, 163–169 (2020).
14. Lin, Z. et al. Flatbands and emergent ferromagnetic ordering in Fe₃Sn₂ kagome lattices. *Phys. Rev. Lett.* **121**, 096401 (2018).
15. Ye, L. et al. de Haas-van Alphen effect of correlated Dirac states in kagome metal Fe₃Sn₂. *Nat. Commun.* **10**, 4870 (2019).
16. Guo, H.-M. & Franz, M. Topological insulator on the kagome lattice. *Phys. Rev. B* **80**, 113102 (2009).
17. Mazin, I. I. et al. Theoretical prediction of a strongly correlated Dirac metal. *Nat. Commun.* **5**, 4261 (2014).
18. Kiesel, M. L., Platt, C. & Thomale, R. Unconventional Fermi surface instabilities in the Kagome Hubbard model. *Phys. Rev. Lett.* **110**, 126405 (2013).
19. Di Sante, D. et al. Turbulent hydrodynamics in strongly correlated Kagome metals. *Nat. Commun.* **11**, 3997 (2020).
20. Neupert, T., Denner, M. M., Yin, J.-X., Thomale, R. & Hasan, M. Z. Charge order and superconductivity in kagome materials. *Nat. Phys.* **18**, 137–143 (2022).
21. Korshunov, A. et al. Softening of a flat phonon mode in the kagome ScV₆Sn₆. *Nat. Commun.* **14**, 6646 (2023).
22. Hu, H. et al. Kagome materials I: SG 191, ScV₆Sn₆, flat phonon soft modes and unconventional cdw formation: Microscopic and effective theory. arXiv preprint arXiv:2305.15469 <https://arxiv.org/abs/2305.15469> (2023).
23. Cao, S. et al. Competing charge-density wave instabilities in the kagome metal ScV₆Sn₆. arXiv preprint arXiv:2304.08197 (2023).
24. Lee, S. et al. Nature of charge density wave in kagome metal ScV₆Sn₆. arXiv preprint arXiv:2304.11820 (2023).
25. Kang, M. et al. Charge order landscape and competition with superconductivity in kagome metals. *Nat. Mater.* **22**, 186–193 (2023).
26. Guo, C. et al. Switchable chiral transport in charge-ordered kagome metal CsV₃Sb₅. *Nature* **611**, 461–466 (2022).
27. Nishimoto, S., Nakamura, M., O'Brien, A. & Fulde, P. Metal-insulator transition of fermions on a kagome lattice at 1/3 filling. *Phys. Rev. Lett.* **104**, 196401 (2010).
28. Denner, M. M., Thomale, R. & Neupert, T. Analysis of charge order in the Kagome metal AV₃Sb₅ (A = K, Rb, Cs). *Phys. Rev. Lett.* **127**, 217601 (2021).
29. Feng, X., Zhang, Y., Jiang, K. & Hu, J. Low-energy effective theory and symmetry classification of flux phases on the kagome lattice. *Phys. Rev. B* **104**, 165136 (2021).
30. Park, T., Ye, M. & Balents, L. Electronic instabilities of kagome metals: Saddle points and Landau theory. *Phys. Rev. B* **104**, 035142 (2021).
31. Jiang, Y.-X. et al. Unconventional chiral charge order in kagome superconductor KV₃Sb₅. *Nat. Mater.* **20**, 1353–1357 (2021).
32. Liang, Z. et al. Three-dimensional charge density wave and surface-dependent vortex-core states in a kagome superconductor CsV₃Sb₅. *Phys. Rev. X* **11**, 031026 (2021).
33. Teng, X. et al. Discovery of charge density wave in a kagome lattice antiferromagnet. *Nature* **609**, 490–495 (2022).
34. Wu, X. et al. Nature of unconventional pairing in the Kagome superconductors AV₃Sb₅ (A = K, Rb, Cs). *Phys. Rev. Lett.* **127**, 177001 (2021).
35. Kang, M. et al. Twofold van Hove singularity and origin of charge order in topological kagome superconductor CsV₃Sb₅. *Nat. Phys.* **18**, 301–308 (2022).
36. Ortiz, B. R. et al. CsV₃Sb₅: a Z₂ topological kagome metal with a superconducting ground state. *Phys. Rev. Lett.* **125**, 247002 (2020).
37. Yu, F. H. et al. Unusual competition of superconductivity and charge-density-wave state in a compressed topological kagome metal. *Nat. Commun.* **12**, 3645 (2021).
38. Du, F. et al. Pressure-induced double superconducting domes and charge instability in the kagome metal KV₃Sb₅. *Phys. Rev. B* **103**, L220504 (2021).
39. Oey, Y. M. et al. Fermi level tuning and double-dome superconductivity in the kagome metal CsV₃Sb_{5-x}Sn_x. *Phys. Rev. Mater.* **6**, L041801 (2022).
40. Li, H. et al. Observation of unconventional charge density wave without acoustic phonon anomaly in Kagome superconductors AV₃Sb₅ (A = Rb, Cs). *Phys. Rev. X* **11**, 031050 (2021).
41. Wang, Z. et al. Electronic nature of chiral charge order in the kagome superconductor CsV₃Sb₅. *Phys. Rev. B* **104**, 075148 (2021).
42. Zhao, H. et al. Cascade of correlated electron states in the kagome superconductor CsV₃Sb₅. *Nature* **599**, 216–221 (2021).
43. Ortiz, B. R. et al. Fermi surface mapping and the nature of charge-density-wave order in the kagome superconductor CsV₃Sb₅. *Phys. Rev. X* **11**, 041030 (2021).
44. Nie, L. et al. Charge-density-wave-driven electronic nematicity in a kagome superconductor. *Nature* **604**, 59–64 (2022).
45. Zhang, X. et al. Destabilization of the charge density wave and the absence of superconductivity in ScV₆Sn₆ under high pressures up to 11 GPa. *Materials* **15**, 7372 (2022).
46. Yin, J.-X., Lian, B. & Hasan, M. Z. Topological kagome magnets and superconductors. *Nature* **612**, 647–657 (2022).
47. Sun, Z. et al. Observation of topological flat bands in the kagome semiconductor Nb₃Cl₈. *Nano Lett.* **22**, 4596–4602 (2022).
48. Tanaka, M. et al. Topological Kagome Magnet Co₃Sn₂S₂ thin flakes with high electron mobility and large anomalous hall effect. *Nano Lett.* **20**, 7476–7481 (2020).
49. Bolens, A. & Nagaosa, N. Topological states on the breathing kagome lattice. *Phys. Rev. B* **99**, 165141 (2019).
50. Di Sante, D. et al. Flat band separation and robust spin berry curvature in bilayer kagome metals. *Nat. Phys.* **19**, 1135–1142 (2023).
51. Tomeljak, A. et al. Dynamics of photoinduced charge-density-wave to metal phase transition in K_{0.3}MoO₃. *Phys. Rev. Lett.* **102**, 066404 (2009).
52. Yusupov, R. V., Mertelj, T., Chu, J.-H., Fisher, I. R. & Mihailovic, D. Single-particle and collective mode couplings associated with 1- and 2-directional electronic ordering in metallic RTe₃ (R=Ho, Dy, Tb). *Phys. Rev. Lett.* **101**, 246402 (2008).
53. Pokharel, A. R. et al. Dynamics of collective modes in an unconventional charge density wave system BaNi₂As₂. *Commun. Phys.* **5**, 141 (2022).
54. Möhr-Vorobeva, E. et al. Nonthermal melting of a charge density wave in TiSe₂. *Phys. Rev. Lett.* **107**, 036403 (2011).
55. Ravnik, J., Vaskivskiy, I., Mertelj, T. & Mihailovic, D. Real-time observation of the coherent transition to a metastable emergent state in 1T-TaS₂. *Phys. Rev. B* **97**, 075304 (2018).
56. Eichberger, M. et al. Snapshots of cooperative atomic motions in the optical suppression of charge density waves. *Nature* **468**, 799–802 (2010).
57. Tomeljak, A. et al. Femtosecond nonequilibrium dynamics in quasi-1d cdw systems K_{0.3}MoO₃ and RB_{0.3}MoO₃. *Phys. B: Condensed Matter* **404**, 548–551 (2009).
58. Huber, T. et al. Coherent structural dynamics of a prototypical charge-density-wave-to-metal transition. *Phys. Rev. Lett.* **113**, 026401 (2014).
59. Storeck, G. et al. Structural dynamics of incommensurate charge-density waves tracked by ultrafast low-energy electron diffraction. *Struct. Dyn.* **7**, 034304 (2020).
60. Demsar, J., Biljaković, K. & Mihailovic, D. Single particle and collective excitations in the one-dimensional charge density wave solid K_{0.3}MoO₃ probed in real time by femtosecond spectroscopy. *Phys. Rev. Lett.* **83**, 800–803 (1999).
61. Chen, R. Y., Zhang, S. J., Zhang, M. Y., Dong, T. & Wang, N. L. Revealing extremely low energy amplitude modes in the charge-density-wave compound LaAgSb₂. *Phys. Rev. Lett.* **118**, 107402 (2017).
62. Yusupov, R. et al. Coherent dynamics of macroscopic electronic order through a symmetry breaking transition. *Nat. Phys.* **6**, 681–684 (2010).
63. Yoshikawa, N. et al. Ultrafast switching to an insulating-like metastable state by amplitude excitation of a charge density wave. *Nat. Phys.* **17**, 909–914 (2021).
64. Schaefer, H. et al. Dynamics of charge density wave order in the quasi one dimensional conductor (TaSe₄)₂I probed by femtosecond optical spectroscopy. *Eur. Phys. J. Spec. Top.* **222**, 1005–1016 (2013).
65. Stojchevska, L. et al. Mechanisms of nonthermal destruction of the superconducting state and melting of the charge-density-wave state by femtosecond laser pulses. *Phys. Rev. B* **84**, 180507 (2011).
66. Pokharel, G. et al. Highly anisotropic magnetism in the vanadium-based kagome metal tbv₆sn₆. *Phys. Rev. Mater.* **6**, 104202 (2022).
67. Hu, Y. et al. Phonon promoted charge density wave in topological kagome metal ScV₆Sn₆. arXiv preprint arXiv:2304.06431 <https://arxiv.org/abs/2304.06431> (2023).
68. Pokharel, G. et al. Highly anisotropic magnetism in the vanadium-based kagome metal TbV₆Sn₆. *Phys. Rev. Mater.* **6**, 104202 (2022).
69. Giannozzi, P. et al. Quantum espresso toward the exascale. *J. Chem. Phys.* **152**, 154105 (2020).
70. Giannozzi, P. et al. Quantum espresso: a modular and open-source software project for quantum simulations of materials. *J. Phys. Condens. Matter* **21**, 395502 (2009).
71. Giannozzi, P. et al. Advanced capabilities for materials modelling with quantum espresso. *J. Phys. Condens. Matter* **29**, 465901 (2017).
72. Perdew, J. P., Burke, K. & Ernzerhof, M. Generalized gradient approximation made simple. *Phys. Rev. Lett.* **77**, 3865–3868 (1996).
73. Hamann, D. R. Optimized norm-conserving Vanderbilt pseudopotentials. *Phys. Rev. B* **88**, 085117 (2013).
74. Wang, V., Xu, N., Liu, J.-C., Tang, G. & Geng, W.-T. VASPKIT: a user-friendly interface facilitating high-throughput computing and analysis using VASP code. *Comput. Phys. Commun.* **267**, 108033 (2021).
75. Momma, K. & Izumi, F. VESTA: a three-dimensional visualization system for electronic and structural analysis. *J. Appl. Crystallogr.* **41**, 653–658 (2008).
76. Consiglio, A. et al. Van hove tuning of AV₃Sb₅ kagome metals under pressure and strain. *Phys. Rev. B* **105**, 165146 (2022).

Acknowledgements

The authors acknowledge Andrea Cavalleri for the fruitful discussions on this work. The research leading to these results has received funding from the European Union's Horizon 2020 research and innovation program under the Marie Skłodowska-Curie

Grant Agreement No. 897276. We gratefully acknowledge the Gauss Center for Supercomputing e.V. (<https://www.gauss-centre.eu>) for funding this project by providing computing time on the GCS Supercomputer SuperMUC-NG at Leibniz Supercomputing Centre (<https://www.lrz.de>). We are grateful for funding support from the Deutsche Forschungsgemeinschaft (DFG, German Research Foundation) under Germany's Excellence Strategy through the Würzburg-Dresden Cluster of Excellence on Complexity and Topology in Quantum Matter ct.qmat (EXC 2147, Project ID 390858490) as well as through the Collaborative Research Center SFB 1170 ToCoTronics (Project ID 258499086) and the Hamburg Cluster of Excellence "CUI: Advanced Imaging of Matter" (EXC 2056, Project No. 390715994). This work has been performed in the framework of the Nanoscience Foundry and Fine Analysis (NFFA-MUR Italy Progetti Internazionali) facility. The Flatiron Institute is a division of the Simons Foundation. S.D.W. and G.Po. acknowledge support via the UC Santa Barbara NSF Quantum Foundry funded via the Q-AMASE-i program under award DMR-1906325. F.M. greatly acknowledges the SoE action of pnrr, number SOE_0000068. I.Z. acknowledges the support from U.S. Department of Energy (DOE) Early Career Award DE-SC0020130.

Author contributions

F.M., D.D.S and F.C. conceived and designed the project. G.Po. and S.D.W. grew the crystals. F.M., C.B. and P.C. carried out the ARPES measurements, while F.C., M.T. and D.P. obtained the pump and probe results. A.C. and S.E. performed the numerical calculations and theoretical analysis supervised by D.D.S, G.S., T.W. and R.T.; D.P., S.E., P.O., W.B., F.P., V.P., P.D.C.K., J.W.W., I.Z., G.R., J.F., I.V., G.P. participated in the discussion and contributed to the writing of the manuscript.

Competing interests

The authors declare no competing interests. Ilija Zeljkovic is a Guest Editor for Communications Materials and was not involved in the editorial review of, or the decision to publish, this Article.

Additional information

Supplementary information The online version contains supplementary material available at <https://doi.org/10.1038/s43246-023-00430-y>.

Correspondence and requests for materials should be addressed to Federico Cilento, Domenico Di Sante or Federico Mazzola.

Peer review information *Communications Materials* thanks the anonymous reviewers for their contribution to the peer review of this work. Primary Handling Editor: Aldo Isidori. A peer review file is available.

Reprints and permission information is available at <http://www.nature.com/reprints>

Publisher's note Springer Nature remains neutral with regard to jurisdictional claims in published maps and institutional affiliations.



Open Access This article is licensed under a Creative Commons Attribution 4.0 International License, which permits use, sharing, adaptation, distribution and reproduction in any medium or format, as long as you give appropriate credit to the original author(s) and the source, provide a link to the Creative Commons license, and indicate if changes were made. The images or other third party material in this article are included in the article's Creative Commons license, unless indicated otherwise in a credit line to the material. If material is not included in the article's Creative Commons license and your intended use is not permitted by statutory regulation or exceeds the permitted use, you will need to obtain permission directly from the copyright holder. To view a copy of this license, visit <http://creativecommons.org/licenses/by/4.0/>.

© The Author(s) 2023